Zeitschrift für anorganische und allgemeine Chemie

Journal of Inorganic and General Chemistry
ZAAC
Zeitschrift für anorganische und allgemeine Chemie

RESEARCH ARTICLE OPEN ACCESS

Delamination of Vermiculite into Ultrahigh-Aspect-Ratio Nanosheets

Felix Uhlig[1] | Alexander M. Stich[1] | Kevin Hagmann[2] | Sabine Rosenfeldt[3] | Josef Breu[1]

[1]Faculty of Biology, Chemistry & Earth Sciences Chair of Inorganic Colloids for Electrochemical Energy Storage, University of Bayreuth, Bayreuth, Germany | [2]BYK Chemie-GmbH, Moosburg, Germany | [3]Faculty of Biology, Chemistry & Earth Sciences Physical Chemistry 1, University of Bayreuth, Bayreuth, Germany

Correspondence: Josef Breu (josef.breu@uni-bayreuth.de)

Received: 23 January 2026 | **Revised:** 23 March 2026 | **Accepted:** 1 April 2026

Keywords: barrier coating | clay | colloids | delamination | vermiculite monolayers

ABSTRACT

The applicability of sustainable materials in the packaging industry is currently limited by the poor gas barrier performance of most biodegradable polymers. Incorporation of high–aspect-ratio nanosheet fillers can significantly enhance barrier properties, yet large-scale production of such fillers remains challenging. Here, we report a gentle route to produce vermiculite (VMT) nanosheets with unprecedented aspect ratios exceeding 10,000 via one-dimensional (1D) dissolution. Complete ion exchange was achieved using citrate as complexing agent, which efficiently removed the pristine interlayer Mg^{2+} and enabled quantitative exchange with monovalent cations. Intercalation with bulky organocations resulted in spontaneous 1D dissolution of VMT in water, yielding translucent, birefringent gels of delaminated nanosheets in up to 71% yield. Structural and morphological analysis by X-ray diffraction (XRD), small-angle X-ray scattering (SAXS), and atomic force microscopy (AFM) confirmed the formation of monolayer nanosheets with lateral sizes exceeding 10 µm. The combination of citrate-assisted exchange and mild spontaneous delamination preserves the intrinsic crystal diameter, enabling aspect ratios that surpass previously reported benchmarks for natural clays. The performance of these nanosheets as barrier pigments showed a remarkable potential for future applications in environmentally friendly packaging.

1 | Introduction

Global plastic waste reached approximately 220 million tons in 2024, with nearly 40% originating from packaging [1]. This persistent waste stream represents a major environmental concern, as microplastics pose severe ecological hazards [2, 3]. In response, biodegradable or water-soluble (bio-)polymers such as polylactic acid, poly(vinyl alcohol), and cellulose derivatives have been extensively investigated as sustainable alternatives [4]. However, most degradable packaging materials exhibit high permeabilities for oxygen and moisture, which hampers best before dates [5]. A promising approach to improve these barrier properties is the incorporation of impermeable nanosheets as fillers into polymer films, which introduce tortuous diffusion pathways and thereby suppress gas and vapor permeation [6–8]. The performance of such fillers is governed by their aspect ratio (diameter/thickness ratio), implying a high potential for nanosheets from clay minerals due to their monolayer thickness of only ~ 1 nm [9]. The improvement of permeability (P_{rel}) of the neat polymer (P_0) is a nonlinear interrelation between aspect ratio of the filler (α), filler content (φ), and a geometric constant (μ), as given in Cussler's Equation (1):

$$P_{rel} = \frac{P}{P_0} = \left(1 + \mu\left(\frac{\alpha^2\varphi^2}{1-\varphi}\right)\right)^{-1} \quad (1)$$

Dedicated to Professor Claus Feldmann on the occasion of his 60th birthday.

Hence, the aspect ratio of the filler becomes the determining quality criterion for the barrier performance of nanosheet fillers.

Setting the conditions right for ionic layered compounds like layered silicates, a spontaneous, thermodynamically driven delamination into monolayers may be realized [10, 11]. (In this paper, we abstain from using delamination and exfoliation as synonyms but rather strictly follow Lagaly's definition, where delamination refers to a process producing monolayers and exfoliation produces thinned tactoids [12].) Basically, once the interlayer height is increased beyond a certain threshold, the entropy of interlayer entities overcomes the attraction of anionic layers and interlayer cations [11]. For this to happen, interlayer cations must segregate to the Helmholtz layers on both sides of the interlayer space. This only works for monovalent cations, as divalent cations reside in the middle of the interlayer and thus block delamination. For low charge densities of the anionic layers, like with smectites, such as sodium-montmorillonite (MMT) or synthetic sodium-fluorohectorite (Hec, $Na_{0.5}[Mg_{2.5}Li_{0.5}]^{oct}[Si_4]^{tet}O_{10}F_2$), in combination with cations offering sufficient hydration enthalpy, like Li^+ or Na^+, hydration of interlayer cations is sufficient to take the system over the threshold separation [13, 14]. With higher charge densities, like with VMTs, bulky yet hydrophilic organocations are needed to open the interlayer space beyond the threshold separation by exerting steric stress [15].

As a result, the layered silicate platelets disintegrate along their stacking axis, analogous to the aqueous dissolution of an ordinary ionic compound. The appeal of this route is the preservation of the initial diameter of the pristine clay platelet. Among the natural 2:1 layered silicates, the charge density of MMT is low enough to allow for spontaneous delamination in its monoionic Na-form. MMT is affordable due to its natural abundance but typically comes in diameters <200 nm, which leads to only mediocre barrier improvements. Synthetic clay minerals like Hec readily produce nanosheets with aspect ratios of ~20,000. However, challenging synthesis conditions lead to high cost [16].

Natural VMT is an attractive alternative candidate given its abundance, low cost (≈200 USD/t), and large crystal size [17]. VMT thus offers the potential to produce large aspect ratio nanosheets with exceptionally high aspect ratios at affordable costs [11].

Several strategies have been suggested to drive exfoliation of VMT, typically by either weakening interlayer interactions and/or applying strong mechanical forces [18, 19]. Methods such as high-shear milling [20–22] or ultrasonication [23, 24] produce thinned tactoids. Exfoliation, however, works at a state where adjacent monolayers in the stack adhere to each other. These shear-induced exfoliation approaches can be assisted by ion exchange with monovalent cations of high hydration enthalpy, such as substitution of Mg^{2+} by Li^+. The brute force impact not only drives thinning but also substantial breakage of platelets, resulting in aspect ratios that fall way behind the values expected from the diameter of the pristine VMT. For instance, in MicroLite patents, VMTs were treated with high shear forces in the presence of Li^+, which resulted in exfoliated tactoids with typical aspect ratio of ≈ 500 [25, 26].

Alternatively, internal pressure can be utilized to separate adjacent layers. VMTs popped by flash evaporation of interlayer water are long known as laboratory adsorbents. Intercalation of hydrogen peroxide followed by heating or ultrasonication also generates high internal gas pressures that promote partial exfoliation [27, 28]. These internal pressure protocols, however, also substantially break platelets and thus fall short of maximizing aspect ratio.

Pristine Mg-vermiculite (Mg-VMT) is incapable of spontaneous delamination by 1D dissolution for two reasons. Firstly, the charge density of VMT is too high to overcome the threshold separation, just because of the hydration forces of the interlayer cation. Secondly, as a divalent cation, Mg^{2+} will reside in the middle of the interlayer, evenly interacting with both adjacent silicate layers and therefore blocking delamination. In this line, Walker first converted VMT to its Na-form, followed by ion exchange with bulky butylammonium that eventually resulted in delamination into a gel [12, 29, 30]. Unfortunately, the selectivity of Mg^{2+} for the interlayer is too high to achieve a complete ion exchange directly with butylammonium. Walker first had to obtain monoionic Na-VMT by changing the exchange solution repeatedly over a period of more than a year. In the second step, Na^+ could then be exchanged for butylammonium to trigger delamination into a gel.

Recently, a one-step process was established, where the equilibrium of the Mg^{2+} exchange was shifted substantially by adding a complexation agent. Different carboxylic acids were investigated, and it was found that citric acid (Cit) with a complexation constant of $\log K_{MgCit^-} = 3.3$ [31] allowed a complete ion exchange for butylammonium by refluxing the Mg-VMT for 1 day. When reducing the ionic strength after ion exchange to levels below 0.05 M by repeated washing followed by centrifugation, the organo-VMT spontaneously delaminated [11].

In this study, delamination-relevant properties like crystallinity, swelling behavior, and layer charge, as well as the influence of the applied organocations, were characterized for the formation of VMT nanosheets. The resulting organo-exchanged VMT could be delaminated by 1D dissolution and produced extraordinarily high aspect ratios of ~ 10,000, which represents a benchmark for natural clay mineral nanosheets and highlights their potential as low-cost, barrier fillers in sustainable packaging.

2 | Results and Discussion

1D dissolution of layered materials depicts the gentle overcoming of electrostatic adhesive forces within two-dimensional, crystalline precursors. The efficiency of this process is strongly influenced by the nature of the interlayer cations, particularly their charge-equivalent area, hydration enthalpy, and valency, as well as the intrinsic properties of the crystalline layers, such as layer charge and charge homogeneity. The layer charge dictates the overall electrostatic attraction, while charge heterogeneity corresponds to localized domains of varying charge density. These domains display nonuniform intracrystalline behavior, which can hamper delamination and rather result in incomplete exfoliation. Synthetic Hec represents an ideal benchmark regarding homogeneity as a result of prolonged annealing at 1045°C. It exhibits an exceptionally uniform charge distribution, which enables spontaneous and complete 1D dissolution in water [16, 32]. Naturally occurring minerals, by contrast, will inevitably display structural imperfections and moderate charge variability. Therefore, charge homogeneity represents a decisive parameter that determines whether a natural mineral can undergo efficient

1D dissolution and thus serve as a precursor of high-aspect ratio nanosheets.

2.1 | Mineralogical Characterization

VMT originates from biotite or phlogopite micas; the latter are formed under high temperature and pressure in the earth's crust, resulting in good crystallinity and surpassingly uniform isomorph substitution of structural ions [33]. Structural iron is oxidized during the transformation to VMT, leading to a substantial reduction of charge density, while at the same time, the potassium interlayer cations are replaced by magnesium. The high hydration enthalpy of the latter yields hydrated interlayers in ambient humid conditions, and thus the interlayer is accessible for alterations like ion exchange [34, 35]. Completion of this transformation is critical because nonoxidized, nonswelling domains pin adjacent silicate layers together, hampering spontaneous delamination. Complete oxidation typically comes with a homogeneous charge density, while complete K^+ exchange assures homogeneous swelling behavior. Both features are essential for successful delamination by 1D dissolution.

Primary particles of raw, milled VMT showed irregular plates with typical dimensions of several tens of micrometers (Figure 1a), making them ideal precursors for producing large, high-quality nanosheets. The sample displays a rational *00l* series with a basal spacing of 14.4 Å consistent with magnesium dihydrate interlayers (Figure 1b). The basal reflection's coefficient of variation (C_V) of 0.05% indicates uniform swelling. An 11- band centered around ~ 20° 2θ and sharp symmetrical reflections around ~ 35° 2θ with $k = 3n$ indicate ± 0.333 *b* planar disorder (Table S1). Reflections typical for residual biotite, for quartz, or for fibrous asbestos-type minerals such as grunerite were below detection limit (inset Figure 1b). Screening for fibrous morphologies in scanning electron microscopy (SEM) micrographs (Figure 1a) was also negative. Needless to say, even traces of asbestos would be an exclusion criterion for food packaging.

Complete biotite weathering is further indicated by the absence of detectable K^+ lines in the energy-dispersive X-ray spectrum (Figure S1, Table S2). Mößbauer spectroscopy, furthermore, confirms full oxidation of octahedral Fe^{2+}. No tetrahedral Fe^{+3} was detected; all structural Fe is present as octahedral Fe^{3+} with a chemical shift of 0.264 mm/s and a quadrupole splitting of 0.561 mm/s (Figure 1c), consistent with reported values for Fe^{3+} in the octahedral sites of weathered VMT [36–38]. In summary, the observed phase purity, complete Fe oxidation, and ample K^+ removal demonstrate full conversion of biotite mica to uniformly hydrated VMT, meeting essential criteria for subsequent delamination via 1D dissolution.

2.2 | Ion-Exchange and Swelling Behavior

To achieve gentle delamination of VMT, it is necessary to completely remove the interlayer Mg^{2+}, as it creates strong and symmetrical electrostatic forces within the stack. This is, however, nontrivial due to the high selectivity of Mg^{2+} compared to monovalent cations like Li^+, Na^+, or even hygroscopic organocations like n-butylammonium [29]. Ample replacement of interlayer Mg^{2+}, as reported by Walker, therefore requires multiple exchange steps applying high reagent excess, which inevitably drives process cost and broader applicability.

Recently, it was shown that adding strong complexing agents for Mg^{2+} can dramatically shift the equilibrium of the exchange reaction [11]. Ligands with sufficient complexation strength effectively remove aqueous Mg^{2+} from the exchange equilibrium, enabling rapid and complete ion exchange. Among such ligands, citric acid stands out as a low-cost chelating agent with an excellent complex formation constant of $\log K_{MgCit^-} = 3.3$, outperforming comparable ligands such as lactate ($\log K_{MgLac^+} = 1.1$) and aspartate ($\log K_{MgAs^+} = 2.6$) [39]. Citric acid is also favorable in the context of food packaging as it is nontoxic and free from respective regulatory restrictions [40].

The efficiency of the citrate-assisted approach is demonstrated by the simple ion exchange of raw VMT in only two exchange steps with a 0.01 M Na_3Cit solution. Conversion to Na-VMT is confirmed by the disappearance of the initial 14.4 Å basal reflection and the appearance of characteristic Na-VMT hydration steps at 9.7, 12.0, and 14.9 Å, representing the zero-, mono-, and bilayer hydrate, respectively, obtained by drying at 100°C, equilibration at 20% RH, and immersion in liquid water (fully hydrated, Figure 2a) [41, 42]. Low C_Vs indicate a rational *00l* series, which in turn is in line with homogeneous intracrystalline swelling behavior. The uniform swelling as a function of water activity

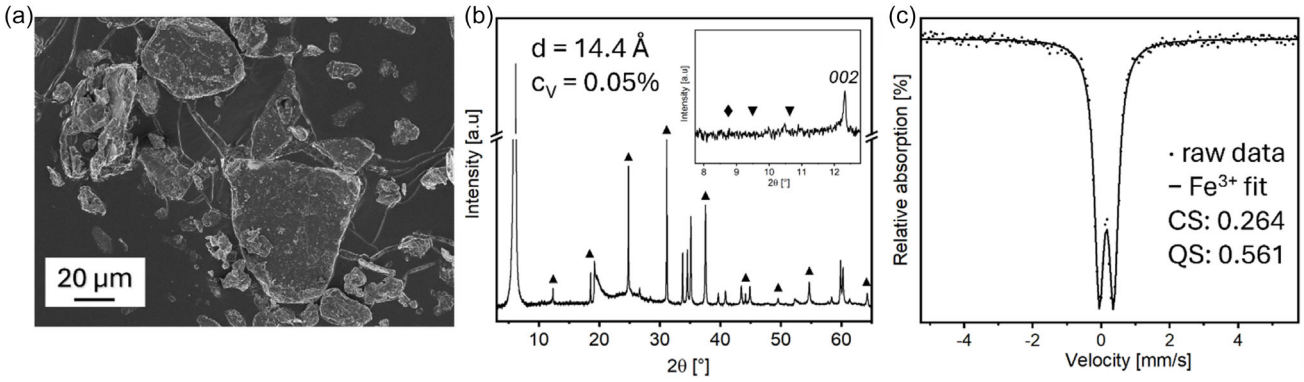

FIGURE 1 | Morphological and structural characterization of raw VMT. (a) Primary particles appear with typical diameters between 10–50 µm. (b) XRD shows high crystallinity with complete absence of side phases like biotite, quartz, or asbestos. A rational *00l* series (▲) with a C_V of 0.05% indicates a uniform swelling/hydration of all interlayers. The inset stresses the absence of characteristic reflections of biotite (♦) or fibrous asbestos (▼). (c) Mößbauer spectra show complete oxidation of structural iron to Fe^{3+}, indicating completion of the weathering process.

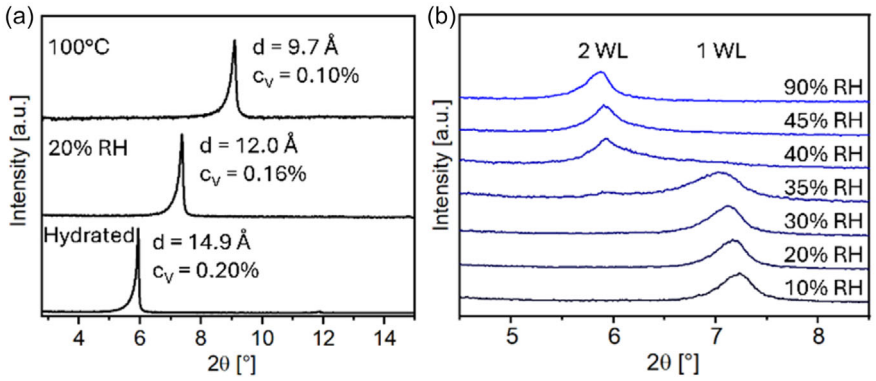

FIGURE 2 | Swelling behavior after citrate-assisted Na exchange. (a) XRDs of zero- (top), mono- (middle), and bilayer hydrate (bottom) Na-VMT. (b) The mono- to bilayer hydrate phase transition is observed from 35 to 40% RH.

is, moreover, reflected by a rather sharp, stepwise transition from mono- to bilayer hydrates observed between 35 and 40% RH (Figure 2b). This transition humidity for Na-VMT was previously observed for a layer charge of $\xi > 0.7\,e^-/(Si, Al)_4O_{10}$ [42].

2.3 | Cation Exchange Capacity and Composition

The supernatant collected after ion exchange contained Al^{3+} and Fe^{3+} in addition to the expected Mg^{2+}, yielding a combined cation exchange capacity of 199 cmol(+)/kg (Table 1). Due to the higher acidity of the aquocomplexes, these trivalent cations tend to form polyoxohydroxy species upon condensation within the interlayer [43–45]. These polyoxohydroxy species typically show high stability in the pH range of 7–9 and require strong chelating ligands for the trivalent ions to accomplish complete exchange. Moreover, the cationic charge of polyoxohydroxy is substantially lower than that of individual hexaquocations. Therefore, simply summing up the charges of exchanged cations found in the supernatant is overestimating the cation exchange capacity (CEC) [44].

As for hexaquocomplexes and polyoxohydroxy islands, the same *d*-values of 14.4 Å are found; the presence of the latter cannot be sensed by XRD. Complex building constants for citric acid with Al^{3+} and Fe^{3+} are substantial ($\log K_{AlCit} = 10.7$ and $\log K_{FeCit} = 11.2$) [46, 47]. Na-citrate is therefore capable of dissolving polyoxohydroxy species and accomplishing complete exchange. Complexation of citrate to Mg^{2+} is weaker than for trivalent cations and requires a pH of 9 for efficient removal of interlayer Mg^{2+} [31].

Monoionic Na-VMT was then applied to determine the real CEC. Photometric analysis by $[Co(trien)]^{3+}$ exchange gave a CEC of 186 cmol(+)/kg (Equation S1), as expected, significantly below the CEC of 199 cmol(+)/kg determined by the number of ions in the supernatant, confirming polyoxohydroxy species in the interlayer. The CEC was cross-checked by thermogravimetry of butylammonium- and n, n-octyldiammonium-exchanged Na-VMT, which gave respective CECs of 172 and 171 cmol(+)/kg (Figure S3, Table S3). After correcting these values for the different molar masses of the organo-VMT as compared to Na-VMT, CECs of 188 and 187 cmol(+)/kg were calculated.

TABLE 1 | Analysis of supernatant after ion exchange.

	Mg^{2+}	Al^{3+}	Fe^{3+}	Sum
Exchanged amount of ions [cmol(+)/kg]	138	46	15	199

The Na-exchanged VMT furthermore allowed the determination of the chemical composition by microprobe analysis to be $[Na_{0.75}]^{inter}[Mg_{2.5}Fe_{0.5}]^{oct}[Si_{2.75}Al_{1.25}]^{tet}O_{10}(OH)_2$. In combination with the analysis of the supernatant of the ion exchange, for the pristine VMT the formula $[Mg_{0.28}Al_{0.06}Fe_{0.02}OH_{0.05}]^{inter}[Mg_{2.5}Fe_{0.5}]^{oct}[Si_{2.75}Al_{1.25}]^{tet}O_{10}(OH)_2$ with a mass of 404.10 g per formula unit may be deduced.

2.4 | Layer Charge Density

Variations in charge density create local differences in interlayer attractions and hence directly influence delamination behavior. Therefore, a VMT intended for delamination into large-aspect-ratio nanosheets must be carefully monitored for its charge heterogeneity, and a robust delamination protocol must be designed accordingly. For smectites with a layer charge $\xi \leq 0.6$ per formula unit, complete ion exchange with alkylammonium cations of increasing alkyl chain length triggers a transition from a mono- to a bilayer arrangement of organocations [48]. In the transition zone, charge variations lead to random interstratification and an apparent, gradual shift of the *d*-value that yields information on the inhomogeneity of charge density. For higher charged VMT, however, a paraffin-like arrangement of alkylammonium is preferred [49]. The absence of well-defined transition regions between these configurations prevents an accurate assessment of charge variation. Applying diammonium cations with a much lower charge equivalent area, instead of ammonium cations (Table S4), however, allows the observation of the same mono- to bilayer transition also for more highly charged VMT with $\xi = 0.75$ e^- per formula unit.

This modified Lagaly method using n, n-alkyldiammonium cations of variable chain length, $NH_3(CH_2)_nNH_3^{2+}$ ($2 \leq n \leq 12$) allowed the determination of the charge densities and their heterogeneity.

A gradual increase in basal spacing from 12.7 Å for $n = 2$ to 13.0 Å for $n = 6$ reflects reorientation of the zigzag-shaped alkyl chain within the monolayer of dications (Figure 3a). The transition to a bilayer arrangement commences for $n = 7$ and is finished with $n = 10$ ($d = 15.3$ Å).

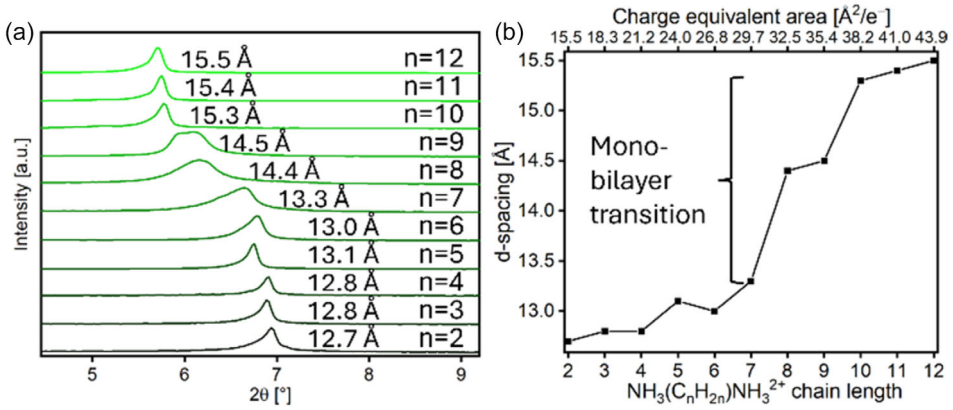

FIGURE 3 | Layer charge heterogeneity determination by the n, n-diammonium method. (a) XRD pattern for diammonium-exchanged VMT with stepwise increase in chain length. (b) Basal spacings plotted against chain length and respective charge-equivalent area.

Based on the equivalent areas, this corresponds to a charge density range of $0.63 < \xi < 0.90$ $e^-/(Si_{2.75}Al_{1.25})_4O_{10}$, (Figure 3b). Despite the uniform swelling behavior, the VMT surprisingly exhibits notable charge heterogeneity. Consequently, the delamination process must account for both low-charge regions, characterized by reduced organocation packing, and high-charge regions, where delamination agents require sufficient hydrophilicity to promote swelling and overcome the strong electrostatic interactions [50, 51]. Failing to address the complete charge density is expected to reduce the yield of delamination.

2.5 | Delamination and Nanosheet Morphology

As outlined earlier, the 1D dissolution of natural VMT with bulky organocations requires an interlayer expansion beyond the threshold in combination with hydrophilic interlayer cations that drive swelling. With highly charged VMT, hydration of interlayer cations like Na^+ is insufficient to take swelling beyond the threshold where entropy contribution wins over Coulomb attraction [41]. Hydration must be supplemented by bulky interlayer cations exerting steric stress because they possess a charge-equivalent area of the organocation (A_{OC}) larger than the underlying charge density of the VMT [13, 15]. When applying binary or tertiary amines as interlayer cations, in addition to a suitable surface area and hydrophilicity, the basicity of organocations must be appreciable, ensuring protonation at pH 9 required for complete removal of Mg^{2+} as citrate complex.

To drive delamination of VMT by spontaneous 1D dissolution, n-butyldiethanolammonium ($BDEA^+$) and megluminium (Meg^+) were employed with respective A_{OC}s of 60 $Å^2/e^-$ and 77 $Å^2/e^-$ (Figure 4a). Their pK_a values of 9.6 and 10 result in 80% and 91% protonation, respectively, under exchange conditions (pH = 9). Both organocations have equivalent areas substantially larger than the lower side of the vermiculite charge density range and thus are expected to exert steric strain upon complete exchange. The ion exchanges were carried out using citrate salts of the ammonium cations at elevated temperatures in two successive exchange steps. Subsequent washing reduced the ionic strength and initiated delamination, yielding translucent gels with 43% yield for BDEA-VMT and 71% for MegVMT, respectively (Table S5). Coarse nondelaminated material settled to the bottom and was separated by decanting.

SAXS patterns of concentrated gels (10 wt% and 13 wt% for BDEA-VMT and MegVMT, respectively) confirmed complete delamination into monolayer nanosheets in the gels, exhibiting a q^{-2}-dependent scattering consistent with a model of dispersed 1 nm-thick disks with diameters of 10 µm (Figure 4b). Pronounced scattering oscillations up to the fourth order indicated nematic liquid–crystalline ordering, revealing uniform nanosheet spacings of 34 nm for BDEA-VMT and 27 nm for Meg-VMT at the respective concentrations. AFM imaging showed intact VMT nanosheets (Figure 4c) with lateral dimensions comparable to those reported for synthetic Hec [16]. Static light scattering (SLS) measurements indicated quite narrow size distributions with mean hydrodynamic radii of 10.3 ± 4.2 µm for BDEA-VMT and 12.2 ± 4.7 µm for MegVMT, respectively (Figure 4d). With a basal thickness of approximately 1 nm, aspect ratios exceeding 10,000 were obtained for both delamination agents, values unprecedented among other natural clay minerals like montmorillonite. Evaporation of the suspensions on glass slides gave textured samples of restacked nanosheets. The larger A_{OC} of Meg corresponds to a larger basal spacing ($d_{001} = 17.8$ Å) compared to BDEA ($d_{001} = 15.9$ Å) (Figure 4e). The gentle delamination of well-crystalline VMT thus produces exceptionally large nanosheets, offering significant potential as high-performance fillers in composite barrier applications.

The barrier enhancement potential of the high-aspect ratio VMT nanosheets was evaluated for a PVOH composite containing 5 vol % filler, demonstrating a significant improvement in the barrier performance. At 23°C and 75% relative humidity, a 5 µm thin coating on a PET substrate (36 µm) exhibited an oxygen transmission rate of 0.08 cm^3 m^{-2} day^{-1}, corresponding to a barrier improvement factor of 200 relative to the neat polymer (Table S6) [52]. These findings highlight the exceptional suitability of VMT nanosheets as functional fillers for high-performance barrier coatings.

2.6 | Implications for Use as Barrier Pigment

The spontaneous delamination by 1D dissolution for VMT in this study offers advantages over conventional exfoliation methods for MMT and VMT, particularly regarding achievable aspect ratios and respective barrier performance (Table 2). In the case

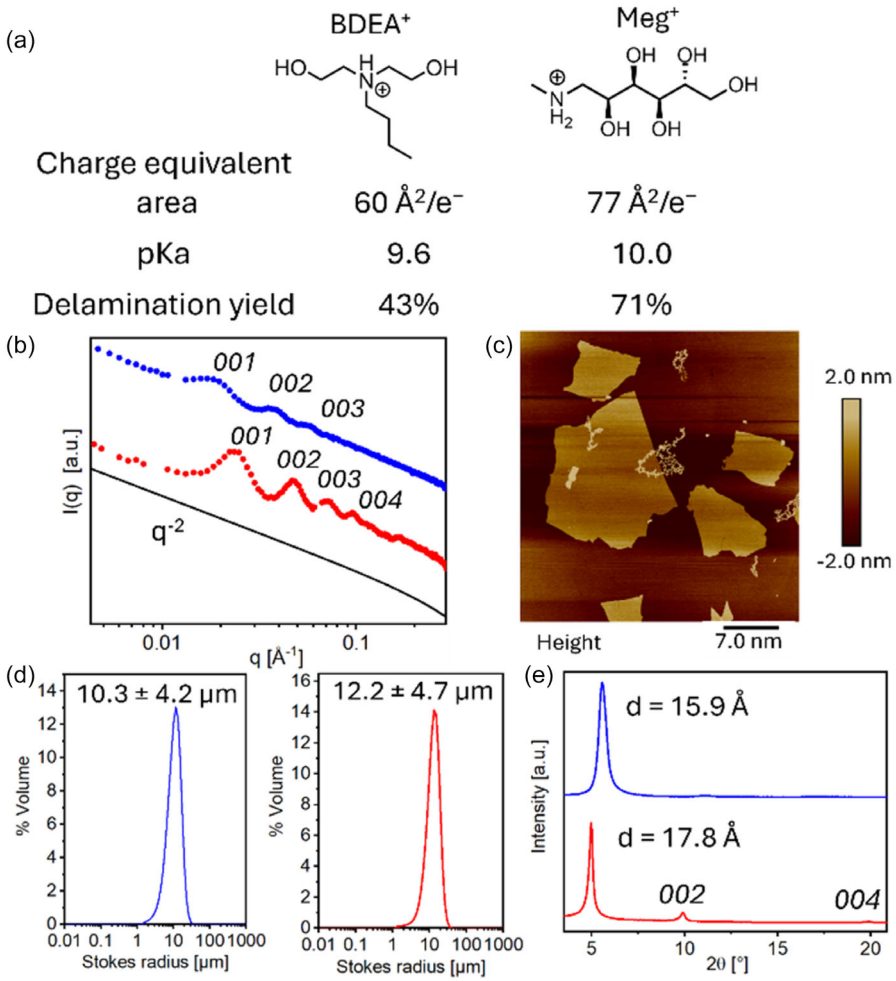

FIGURE 4 | Delamination characteristics of vermiculite. (a) Comparison of Meg^+ and $BDEA^+$ regarding charge equivalent area, pKa, and resulting delamination yield upon twofold exchange. (b) SAXS patterns of concentrated suspensions of BDEA-VMT (blue), Meg-VMT (red), and a calculated pattern for a disk with 1 nm thickness (black). (c) AFM image of delaminated VMT reveals fully delaminated nanosheets. (d) Particle size distribution with average hydrodynamic diameters as determined by SLS. (e) XRDs of dried films of delaminated and then restacked Meg- and BDEA-VMT.

of MMT, the materials have to be first size classified to remove coarse accessory minerals like quartz, followed by chemical removal of amorphous binders like aluminum and iron oxyhydroxides by a dithionite, citrate, bicarbonate treatment [53]. The latter automatically yields the monoionic Na form, which spontaneously delaminates due to the lower charge density compared to vermiculites. While complete delamination takes a comparable effort to 1D dissolution of VMT, the small crystal sizes limit aspect ratios to < 200.

For VMT, the pristine crystal diameters are larger, but the higher charge density and hence stronger electrostatic attraction typically limit the efficiency of brute force exfoliation methods like ultrasonication and high shear milling to the formation of multilayer tactoids. Even when combined with chemical treatment using Li^+, Na^+, or H_2O_2, these methods generally achieve aspect ratios of < 500, thus falling short of exploiting the full potential of VMT for high-aspect-ratio nanosheets.

The 1D dissolution process differs fundamentally from these mechanical or chemical exfoliation techniques in two key aspects that markedly enhance the obtained aspect ratio:

1. The fraction of the material that delaminates (supernatant gel) yields suspensions containing exclusively monolayer nanosheets.
2. he absence of external mechanical forces prevents fracture of the 1 nm-thick sheets and thus maximizes aspect ratio.

Both characteristics are essential for achieving superior barrier performance. A monomodal thickness of nanosheets of maximized aspect ratio promotes a perfectly textured and uniform alignment within polymer matrices. In contrast, multimodal thickness distributions, even at similar aspect ratios, hinder alignment and reduce barrier efficiency [54, 55].

The 1D dissolution proceeds simply through infinite hydration upon immersion in water, Table 2, which overcomes electrostatic interactions without the need for additional external force [11]. This gentle mechanism is critical for maintaining the structural integrity and high aspect ratio of the nanosheets. High-aspect-ratio monolayers would instead tend to fracture readily under shear or cavitation forces encountered in conventional processes [59].

TABLE 2 | Comparison of delamination methods, applied external force, and resulting aspect ratio.

Method	External forces applied	Material	Aspect ratio	Reference
Ultrasonication	high-medium	MMT	30–200	[56]
		VMT	30–200	[23]
High-shear milling	high	MMT	30–150	[57]
		VMT	20–100	[58]
Chemical pretreatment and exfoliation	high-medium	MMT	150–200	[56]
		VMT	< 500	[26]
1D dissolution	very low	Organocation exchanged VMT	> 10,000	this work

As a result, the 1D dissolution route achieves both complete delamination into monolayer nanosheets and preservation of their high aspect ratios. The resulting large-aspect-ratio VMT nanosheets present a promising strategy for enhancing the barrier performance of degradable polymer composites, even under elevated humidity conditions.

3 | Conclusion

The transition toward (bio-)degradable packaging materials has been limited by inadequate barrier properties, while state-of-the-art filler materials have shown restricted potential due to incomplete exfoliation, low aspect ratios, or high production costs. In this context, expanding 1D dissolution to natural VMT with sterically demanding, bulky organocations enables a straightforward way to produce water-based polymer composites with VMT nanosheets of unprecedented aspect ratio. These nanosheets serve as highly efficient barrier pigments, offering a promising pathway toward biodegradable polymer composites suitable for food packaging applications.

4 | Experimental Section

4.1 | Materials

The vermiculite of medium grain size (4.75 − 2 cm) was obtained from BTHS GmbH, Hamburg, Germany, and ground to 80 µm particle size by a rotary mill Pulverisette 14 (Fritzsch, Germany).

Meglumine (Meg) (99%) and n, n-alkyldiamines (>97%) were obtained from Thermo Fisher Scientific; n-butyldiethanolamine (BDEA) (>98.6%), citric acid monohydrate (Cit) (>99.8%), and hydrochloric acid (1 M) by Fisher Chemical; sodium citrate dihydrate (>99%), cobalt^{II}-nitrate hexahydrate (>99.9%), triethylenetetramine (trien) (>97%), and polyvinylic alcohol Mowiol 20–98 ($M_W = 125\ 000$ g mol^{-1}, 98 mol% hydrolyzed) by Sigma Aldrich. All chemicals were used as they were received.

4.2 | Ion Exchange

Na-exchange was accomplished in two exchange steps, applying 0.1 g VMT powder in a Na_3Cit solution (0.01 M, 40 ml, pH = 9) in an overhead shaker for 12 h each, followed by washing in double-distilled water and drying at 40°C.

For exchange with n, n-alkyldiammonium ions with variable chain length (n = 2–12), 0.1 M solutions in water/ethanol (1:1 vol) were obtained by titration with hydrochloric acid (pH = 5 for $n = 2$, pH 6 for $n = 3$, and pH 6–7 for $n = 4$–12). Typically, 20 mg of Na-VMT were exchanged five times in 2 ml solution for 24 h per step, followed by washing five times with water, five times with water/ethanol 1:1, and drying at 40°C.

N-butylammonium exchange was achieved in five exchange steps of at least 8 h each by immersing Na-VMT into a 1 M solution titrated to pH 7 followed by ten washing steps with water/ethanol 1:1.

4.3 | Delamination

Delamination was accomplished upon complete ion exchange of Mg^{2+} (pristine VMT) by either Meg^+- or $BDEA^+$ citrate. 3.72 mmol of the organocations were dissolved in 5 ml double-distilled water and titrated to pH 9 with citric acid. 1 g ground VMT was added and heated to 120°C under reflux conditions for 2 h in a 50 ml round flask. The VMT was separated from the supernatant by centrifugation at 5000 rpm, and the exchange was repeated with a fresh solution under the same conditions. Finally, the organo-VMT was washed with double-distilled water to lower the ionic strength and thus trigger 1D dissolution. As delamination is incomplete, the suspensions were centrifuged at 10 000 rpm for 15 min after 3 days of washing, and the liquid crystalline suspension was decanted from the precipitate. The yield was determined by comparing the solid weight content of the suspensions with the weight of nondelaminated residue.

4.4 | Characterization

4.4.1 | Scanning Electron Microscopy and Energy-Dispersive X-Ray Spectroscopy

Scanning electron microscopy (SEM) micrographs were recorded using the system ZEISS LEO 1530 (Carl Zeiss AG, Germany) operating at 3 kV, equipped with an in-lens secondary electron detector and an UltraDry-EDS-Detector (30 mm^2, Thermo Fisher Scientific). The sample was prepared on carbon tape.

4.4.2 | X-Ray Diffraction

XRD patterns were measured in transmission geometry on a STOE STADI P diffractometer (Ge monochromator, $CuK_{\alpha 1}$

radiation, $\lambda = 1.54059$ Å, 1 mm slit width) in flame-sealed glass capillaries (0.5 mm diameter, Hilgenberg) with a 0.5° 2θ step size and 20 s counting time per step. Raw VMT was measured after milling; Na-exchanged species were equilibrated at 20% RH and room temperature, or at 100°C, respectively, for at least 2 days.

X-ray diffraction patterns of textured flat film samples were measured in Bragg–Brentano geometry on an Xpert Pro (Malvern Panalytical, Netherlands) equipped with a PixCel1D-Medipix3 detector (CuK_α radiation, $\lambda = 1.54178$ Å, nickel filter), a slit width of 1/8 in. 0.028° 2θ step size, and 180 s counting time per step. The swelling behavior of Na-VMT as a function of relative humidity (10–90% RH) was followed in a temperature-humidity chamber (Malvern Panalytical, Netherlands). Samples were equilibrated for 15 min before each measurement point. Diffraction patterns were analyzed by applying the software HighScore Plus provided by Malvern Panalytical.

4.4.3 | Mößbauer Spectroscopy

Mößbauer spectra were collected using a configuration tailored for high-resolution measurements. The setup included a WissEl Mößbauer Drive System MR-360 coupled with an MA-260 velocity transducer to ensure precise and controlled motion of the [57] Co(Rh) source (activity: ∼2 GBq) and a KETEK silicon drift detector AXAS-M. Gain and shaping time constants were optimized experimentally. Data acquisition was carried out using a CMCA-550 module in MCS [WINDOW] mode, enabling the selective detection of the 14.4 keV Mössbauer line. Calibration was performed with a [57] Fe-enriched metallic foil. Measurements were conducted at room temperature. The sinusoidal velocity waveform for the source motion was generated by a DFG-1000 digital function generator, synchronized with the channel sweep of the CMCA-550. Spectral data were processed and analyzed using MossA software to ensure precise alignment and energy calibration [60].

4.4.4 | Cation Exchange Capacity

The CEC of Na-VMT was determined photometrically by $[Co(trien)]^{3+}$ exchange (for details see SI) with an Agilant Cary 300 (Agilant Technologies, USA). Additionally, the CEC of n-butylammonium and n, n-octyldiammonium-exchanged VMT was determined by thermogravimetry (Table S3) with a Linseis STA PT 1600 (Linseis Messgeräte GmbH, Germany) with a heating rate of 10°C/min under synthetic air.

4.4.5 | Layer Charge Density

Layer charge densities and charge homogeneities were determined by applying a modified Lagaly routine [48]. In order to observe the transition from monolayer to double layer for highly charged VMT, instead of alkylammonium, we applied alkyldiammonium dichloride exchange with varying alkyl chain lengths.

4.4.6 | Chemical Composition

The chemical composition of Na-VMT was determined by wavelength-dispersive X-ray spectroscopy on single crystals using an electron microprobe (Jeol-iSP100, Bayerisches Geoinstitut, Bayreuth). The settings were 15 kV acceleration voltage, 15 nA initial beam current, a beam spot diameter of 1–2 µm, 20 s counting time at the peak positions, and 10 s counting time at each side of the peaks. The sample was embedded in a polymer matrix before being polished.

Mg, Al, and Fe released during ion exchange were determined by flame atomic absorption spectroscopy on a Varian AA100 (Varian, USA). The exchange and washing supernatants were collected, dried at 100°C, pyrolyzed at 450°C to remove excessive organic content, and redissolved in 1 M HCl prior to flame atomic absorption spectroscopy.

4.4.7 | Small-Angle X-Ray Scattering

Prior to the measurement, delaminated Meg- and BDEA-VMT were concentrated by centrifugation to 13 wt% and 10 wt%, respectively. SAXS data were measured using a "Double Ganesha AIR" (SAXSLAB/Xenocs). The X-ray source of this laboratory-based system is a rotating copper anode (MicroMax 007HF, Rigaku Corporation, Japan). The data were recorded by a position-sensitive detector (PILATUS 300 K, Dectris). The suspensions were measured in 1-mm glass capillaries (Hilgenberg). The circularly averaged data are normalized to the incident beam, sample thickness, and measurement time. Background subtraction was performed by using the SAXS pattern of a water-filled capillary for the suspensions. Further evaluation was performed with the software Scatter (Version 2.5) [61].

4.4.8 | Atomic Force Microscopy

Atomic force microscopy was performed on a Nano-scope Dimension 3100 (Bruker Nano Inc.) in tapping mode in air. An OTESPA-R3-cantilever (Bruker Nano Inc.) was used, which has a resonance frequency of 300 kHz and a typical spring constant of 26 nm^{-1}. AFM images were processed with NanoScope Analysis 1.80 (Bruker Nano Inc.). The samples were prepared by dropcasting a diluted nanosheet suspension (10 mg/L) on a 1x1 cm^2 silicon wafer (PLANO) that was cleaned with analytical grade ethanol, followed by "snow jetting" with a CO_2 gun and oxygen plasma treatment.

4.4.9 | Static Light Scattering

The hydrodynamic diameter (Stokes-Einstein radius) distribution of nanosheet suspensions was determined with a Horiba LA-950 (Retsch, Germany) for aqueous media.

4.4.10 | Barrier Testing

A barrier composite coating was prepared by mixing 0.5 g of a delaminated Meg-VMT suspension (6 wt%) with 5.6 g of a polyvinyl alcohol solution (5 wt%) and 5.1 mL of double-distilled water, first under gentle stirring for 15 min, followed by speed mixing under vacuum (DAC 400.2 VAC-P, Hauschild GmbH & Co., Germany) to remove dissolved gases. The suspension was coated on a corona-pretreated polyethylene terephthalate substrate (36 µm, Bleher Folientechnik, Germany) with an automated doctor blade and 4 mil slit height at 10 mm/s coating speed. The coating was dried at room temperature for 2 h, followed by 4 h at 60°C. Film thickness was determined using a high-accuracy Digimatic micrometer (Mitutoyo, Japan) with a resolution of 0.0001 mm. The oxygen transmission rate at 23°C and 75% RH was determined with an OX-TRAN 2/22 10X (Mocon, Minneapolis, USA) with a lower detection limit of 0.0005 $cm^3m^{-2}day^{-1}$.

Acknowledgments

We thank Marco Schwarzmann for SEM imaging and EDS analysis. We appreciate the support from the Keylabs (Mesoscale Characterization: Scattering Techniques, Surface and Interface Characterization, Electron and Optical Microscopy, and Polymer Additives and Fillers) of the Bavarian Polymer Institute (BPI) at University of Bayreuth. Bayerisches Geoinstitut is acknowledged for microprobe analysis. This research was supported by the Altana Institute.

Open Access funding enabled and organized by Projekt DEAL.

Funding

The project has received funding from the Altana Institute, Deutsche Forschungsgemeinschaft (DFG, German Re-search Foundation) – project number (391977956 – SFB1357/C02).

Conflicts of Interest

The authors declare no conflicts of interest.

Data Availability Statement

The data that support the findings of this study are available from the corresponding author upon reasonable request.

References

1. OECD, *Global Plastics Outlook: Economic Drivers, Environmental Impacts and Policy Options* (OECD Publishing, OECD Publishing, 2022) https://doi.org/10.1787/de747aef-en, https://www.oecd.org/en/publications/global-plastics-outlook_de747aef-en.html.

2. L. An, Q. Liu, Y. Deng, W. Wu, Y. Gao, and W. Ling, "Sources of Microplastic in the Environment," *Microplastics in Terrestrial Environments: Emerging Contaminants and Major Challenges*, ed. D. He and Y. Luo, (Springer International Publishing, 2020): 143–159, https://doi.org/10.1007/698_2020_449.

3. N. Kasmuri, N. A. A. Tarmizi, and A. Mojiri, "Occurrence Impact, Toxicity, and Degradation Methods of Microplastics in Environment—a Review," *Environmental Science and Pollution Research* 29, no. 21 (2022): 30820–30836, https://doi.org/10.1007/s11356-021-18268-7.

4. S. Mangaraj, A. Yadav, L. M. Bal, S. K. Dash, and N. K. Mahanti, "Application of Biodegradable Polymers in Food Packaging Industry: A Comprehensive Review," *Journal of Packaging Technology and Research* 3, no. 1 (2019): 77–96, https://doi.org/10.1007/s41783-018-0049-y-/10.1007/s41783-018-0049-y.

5. S. Shaikh, M. Yaqoob, and P. Aggarwal, "An Overview of Biodegradable Packaging in Food Industry," *Current Research in Food Science* 4 (2021): 503–520, https://doi.org/10.1016/j.crfs.2021.07.005-/10.1016/j.crfs.2021.07.005.

6. E. L. Cussler, S. E. Hughes, W. J. Ward, and R. Aris, "Barrier membranes," *Journal of Membrane Science* 38, no. 2 (1988): 161–174, https://doi.org/10.1016/S0376-7388(00)80877-7-/10.1016/S0376-7388(00)80877-7.

7. Y. Cui, S. Kumar, B. Rao Kona, and D. van Houcke, "Gas Barrier Properties of Polymer/Clay Nanocomposites," *RSC Advances* 5, no. 78 (2015): 63669–63690, https://doi.org/10.1039/C5RA10333A.

8. S. Yue, T. Zhang, S. Wang, et al., "Recent Progress of Biodegradable Polymer Package Materials: Nanotechnology Improving Both Oxygen and Water Vapor Barrier Performance," *Nanomaterials* 14, no. 4 (2024): 338, https://doi.org/10.3390/nano14040338-/10.3390/nano14040338.

9. R. A. Schoonheydt and Y. Clay Umemura, "Minerals as Natural Nanosheets," *In Inorganic Nanosheets and Nanosheet-Based Materials: Fundamentals and Applications of Two-Dimensional Systems*, ed. T. Nakato, J. Kawamata and S. Takagi, (Springer Japan, 2017): 33–53, https://doi.org/10.1007/978-4-431-56496-6_2.

10. M. Daab, S. Rosenfeldt, H. Kalo, et al., "Two-Step Delamination of Highly Charged, Vermiculite-like Layered Silicates via Ordered Heterostructures," *Langmuir* 33, no. 19 (2017): 4816–4822, https://doi.org/10.1021/acs.langmuir.7b01008-/10.1021/acs.langmuir.7b01008.

11. V. Dudko, R. L. Timmins, O. Khoruzhenko, et al., "Spontaneous Delamination of Affordable Natural Vermiculite as a High Barrier Filler for Biodegradable Food Packaging," *Materials Advances* 3, no. 24 (2022): 9052–9062, https://doi.org/10.1039/D2MA00734G.

12. J. E. F. C. Gardolinski and G. Lagaly, "Grafted Organic Derivatives of Kaolinite: II. Intercalation of Primary n-Alkylamines and Delamination," *Clay Minerals* 40, no. 4 (2005): 547–556, https://doi.org/10.1180/0009855054040191.

13. S. Rosenfeldt, M. Stöter, M. Schlenk, et al., "In-Depth Insights into the Key Steps of Delamination of Charged 2D Nanomaterials," *Langmuir* 32, no. 41 (2016): 10582–10588, https://doi.org/10.1021/acs.langmuir.6b02206-/10.1021/acs.langmuir.6b02206.

14. V. Dudko, O. Khoruzhenko, S. Weiß, et al., "Repulsive Osmotic Delamination: 1D Dissolution of 2D Materials," *Advanced Materials Technologies* 8, no. 3 (2023): 2200553, https://doi.org/10.1002/admt.202200553-/10.1002/admt.202200553.

15. M. Daab, N. J. Eichstaedt, A. Edenharter, S. Rosenfeldt, and J. Breu, "Layer Charge Robust Delamination of Organo-Clays," *RSC Advances* 8, no. 50 (2018): 28797–28803, https://doi.org/10.1039/C8RA05318A.

16. M. Stöter, D. A. Kunz, M. Schmidt, et al., "Nanoplatelets of Sodium Hectorite Showing Aspect Ratios of ≈20 000 and Superior Purity," *Langmuir* 29, no. 4 (2013): 1280–1285, https://doi.org/10.1021/la304453h-/10.1021/la304453h.

17. T. J. Brown, *World Mineral Production 2015-2019;*, 2021.

18. S. Hillier, E. M. M. Marwa, and C. M. Rice, "On the Mechanism of Exfoliation of 'Vermiculite'," *Clay Minerals* 48, no. 4 (2013): 563–582, https://doi.org/10.1180/claymin.2013.048.4.01.

19. M. Li, Y. Zhao, Z. Ai, H. Bai, T. Zhang, and S. Song, "Preparation and Application of Expanded and Exfoliated Vermiculite: A Critical Review," *Chemical Physics* 550 (2021): 111313, https://doi.org/10.1016/j.chemphys.2021.111313-/10.1016/j.chemphys.2021.111313.

20. K.Č. Barabaszová and M. Valášková, "Characterization of Vermiculite Particles after Different Milling Techniques," *Powder Technology* 239 (2013): 277–283, https://doi.org/10.1016/j.powtec.2013.01.053-/10.1016/j.powtec.2013.01.053.

21. A. Węgrzyn, W. Stawiński, O. Freitas, et al., "Study of Adsorptive Materials Obtained by Wet Fine Milling and Acid Activation of Vermiculite," *Applied Clay Science* 155 (2018): 37–49, https://doi.org/10.1016/j.clay.2018.01.002-/10.1016/j.clay.2018.01.002.

22. R. B. L. Hanken, R. R. Arimatéia, G. M. G. Farias, et al., "Effect of Natural and Expanded Vermiculite Clays on the Properties of Eco-Friendly Biopolyethylene-Vermiculite Clay Biocomposites," *Composites Part B: Engineering* 175 (2019): 107184, https://doi.org//10.1016/j.compositesb.2019.107184.

23. F. Ali, L. Reinert, J.-M. Levêque, et al., "Effect of Sonication Conditions: Solvent, Time, Temperature and Reactor Type on the Preparation of Micron Sized Vermiculite Particles," *Ultrasonics Sonochemistry* 21, no. 3 (2014): 1002–1009, https://doi.org/10.1016/j.ultsonch.2013.10.010-/10.1016/j.ultsonch.2013.10.010.

24. Y. T. Park, Y. Qian, C. I. Lindsay, et al., "Polyol-Assisted Vermiculite Dispersion in Polyurethane Nanocomposites," *ACS Applied Materials & Interfaces* 5, no. 8 (2013): 3054–3062, https://doi.org/10.1021/am303244j.

25. Douglas P. Karim, G. H.A., and Carrie A. Feeney, *Michele Farrell. Multilayer Nanocomposite Barrier Structures. US*. (2005, https://patents.google.com/patent/US8309230B2

26. Semyon D. Friedman, M. R.W., Chia-Chih Ou, Robert M. Spotnitz, and Shaohai Wu, "Vermiculite Composition with Improved Chemical Exfoliation," *USA*. (1993, https://patents.google.com/patent/US5326500A

27. A. N. Nguyen, L. Reinert, J. M. Lévêque, et al., "Preparation and Characterization of Micron and Submicron-Sized Vermiculite Powders by Ultrasonic Irradiation," *Applied Clay Science* 72 (2013): 9–17, https://doi.org/10.1016/j.clay.2012.12.007-/10.1016/j.clay.2012.12.007.

28. J. Wang, Z. Cui, S. Li, et al., "Unlocking Osmotic Energy Harvesting Potential in Challenging Real-World Hypersaline Environments through Vermiculite-Based Hetero-Nanochannels," *Nature Communications* 15, no. 1 (2024): 608, https://doi.org/10.1038/s41467-023-44434-1.

29. G. F. Walker and W. G. Garrett, "Chemical Exfoliation of Vermiculite and the Production of Colloidal Dispersions," *Science* 156, no. 3773 (1967): 385–387, https://doi.org/10.1126/science.156.3773.385-doi:10.1126/science.156.3773.385.

30. L. F. Braganza, R. J. Crawford, M. V. Smalley, and R. K. Thomas, "Swelling of n-Butylammonium Vermiculite in Water," *Clays and Clay Minerals* 38, no. 1 (1990): 90–96, https://doi.org/10.1346/CCMN.1990.0380112.

31. A. K. Covington and E. Y. Danish, "Measurement of Magnesium Stability Constants of Biologically Relevant Ligands by Simultaneous Use of pH and Ion-Selective Electrodes," *Journal of Solution Chemistry* 38, no. 11 (2009): 1449–1462, https://doi.org/10.1007/s10953-009-9459-3.

32. H. Kalo, W. Milius, and J. Breu, "Single Crystal Structure Refinement of One- and Two-Layer Hydrates of Sodium Fluorohectorite," *RSC Advances* 2, no. 22 (2012): 8452–8459, https://doi.org/10.1039/C2RA20457F-/10.1039/C2RA20457F.

33. Z. Rahnama, S. Hassanpour, D. Savard, and Z. Shah, "Mineral Chemistry of Apatite, Amphibole, Biotite, and Magnetite from the Masjeddaghi Porphyry Cu-Au Deposit, NW Iran: Petrogenetic and Metallogenic Implications," *Frontiers in Earth Science* 13 (2025): 1603296.https://doi.org/10.3389/feart.2025.1603296.

34. M. J. Wilson, "A Study of Weathering in a Soil Derived from a Biotite-Hornblende Rock: I. Weathering of Biotite," *Clay Minerals* 8, no. 3 (1970): 291–303, https://doi.org/10.1180/claymin.1970.008.3.07.

35. E. A. Ferrow, "Experimental Weathering of Biotite, Muscovite and Vermiculite : A Mössbauer Spectroscopy Study," *European Journal of Mineralogy* 14, no. 1 (2002): 85–95, https://doi.org/10.1127/0935-1221/2002/0014-0085.

36. E. A. Ferrow, "Experimental Weathering of Biotite, Muscovite and Vermiculite: A Mössbauer Spectroscopy Study," *European Journal of Mineralogy* 14, no. 1 (2002): 85–95, https://doi.org/10.1127/0935-1221/2002/0014-0085-/10.1127/0935-1221/2002/0014-0085.

37. V. Luca, "Detection of Tetrahedral Fe^{3+} Sites in Nontronite and Vermiculite by Mössbauer Spectroscopy," *Clays and Clay Minerals* 39, no. 5 (1991): 467–477, https://doi.org/10.1346/CCMN.1991.0390502.

38. C. Maqueda, A. S. Romero, E. Morillo, J. L. Pérez-Rodríguez, A. Lerf, and F. E. Wagner, "The behavior of Fe in ground and acid-treated vermiculite from Santa Olalla, Spain," *Clays and Clay Minerals* 56, no. 3 (2008): 380–388, https://doi.org/10.1346/CCMN.2008.0560307.

39. J. L. Meyer, "Formation Constants for Interaction of Citrate with Calcium and Magnesium Lons," *Analytical Biochemistry* 62, no. 1 (1974): 295–300, https://doi.org/10.1016/0003-2697(74)90391-1-/10.1016/0003-2697(74)90391-1.

40. R. Ciriminna, F. Meneguzzo, R. Delisi, and M. Pagliaro, "Citric Acid: Emerging Applications of Key Biotechnology Industrial Product," *Chemistry Central Journal* 11 (2017): 22, https://doi.org/10.1186/s13065-017-0251-y.

41. G. Lagaly, *Volume 1: Handbook of Clay Science*, (Elsevier Science, 2006).

42. S. W. Bailey, *Hydrous Phyllosilicates: (Exclusive of Micas)*, (De Gruyter, 2018).

43. A. Lerf, F. E. Wagner, J. Poyato, and J. L. Pérez-Rodríguez, "Intercalation and Dynamics of Hydrated Fe2+ in the Vermiculites from Santa Olalla and Ojén," *Journal of Solid State Electrochemistry* 15, no. 2 (2011): 223–229, https://doi.org/10.1007/s10008-010-1171-0.

44. R. I. Barnhisel and P. M. Bertsch, "Chlorites and Hydroxy-Interlayered Vermiculite and Smectite," *Minerals in Soil Environments* (Soil Science Society of America, 1989): 729–788, https://doi.org/10.2136/sssabookser1.2ed.c15.

45. J. Dietel, J. Gröger-Trampe, M. Bertmer, S. Kaufhold, K. Ufer, and R. Dohrmann, "Crystal Structure Model Development for Soil Clay Minerals – I. Hydroxy-Interlayered Smectite (HIS) Synthesized from Bentonite. A Multi-Analytical Study," *Geoderma* 347 (2019): 135–149, https://doi.org/10.1016/j.geoderma.2019.03.021-/10.1016/j.geoderma.2019.03.021.

46. M. A. Lopez-Quintela, W. Knoche, and J. Veith, "Kinetics and Thermodynamics of Complex Formation between Aluminium(III) and Citric Acid in Aqueous Solution," *Journal of the Chemical Society, Faraday Transactions 1: Physical Chemistry in Condensed Phases* 80, no. 8 (1984): 2313–2321, https://doi.org/10.1039/F19848002313.

47. T. B. Field, J. L. McCourt, and W. A. E. McBryde, "Composition and Stability of Iron and Copper Citrate Complexes in Aqueous Solution," *Canadian Journal of Chemistry* 52, no. 17 (1974): 3119–3124, https://doi.org/10.1139/v74-458.

48. G. Lagaly and A. Weiss, "Neue Methoden zur Charakterisierung Und Identifizierung Quellungsfähigen Dreischichttonminerale," *Zeitschrift für Pflanzenernährung Und Bodenkunde* 130, no. 1 (1971): 9–24, https://doi.org/10.1002/jpln.19711300103-/10.1002/jpln.19711300103.

49. G. Lagaly, "Layer Charge Heterogeneity in Vermiculites," *Clays and Clay Minerals* 30, no. 3 (1982): 215–222, https://doi.org/10.1346/CCMN.1982.0300308.

50. M. Stevenson, S. Pappler, L. Kanzler, et al., "Ion and Solvent Dynamics in Charged 2D Clay Nanoslits with Unprecedented Ångström-Precise Slit Height Control," *Advanced Functional Materials* n/a, no. n/a (2025): e15706, https://doi.org//10.1002/adfm.202515706.

51. M. Daab, N. J. Eichstaedt, C. Habel, et al., "Onset of Osmotic Swelling in Highly Charged Clay Minerals," *Langmuir* 34, no. 28 (2018): 8215–8222, https://doi.org/10.1021/acs.langmuir.8b00492.

52. M. Röhrl, L. K. S. Federer, R. L. Timmins, et al., "Disorder–Order Transition—Improving the Moisture Sensitivity of Waterborne Nanocomposite Barriers," *ACS Applied Materials and Interfaces* 13, no. 40 (2021): 48101–48109, https://doi.org/10.1021/acsami.1c14246-/10.1021/acsami.1c14246.

53. O. P. Mehra and M. L. Jackson, "Iron oxide removal from soils and clays by a dithionite-citrate system buffered with sodium bicarbonate," *in 7th National Conference on Clays and Clay Minerals*, ed. E. Ingerson, (Pergamon Press, 2013): 317–327, https://doi.org/10.1016/B978-0-08-009235-5.50026-7.

54. V. Mittal, "Modelling and Prediction of Barrier Properties of Polymer Layered Silicate Nanocomposites," *Polymers and Polymer Composites* 21, no. 8 (2013): 509–518, https://doi.org/10.1177/096739111302100804.

55. S. Behr, U. Vainio, M. Müller, A. Schreyer, and G. A. Schneider, "Large-Scale Parallel Alignment of Platelet-Shaped Particles through Gravitational Sedimentation," *Scientific Reports* 5, no. 1 (2015): 9984, https://doi.org/10.1038/srep09984.

56. L. Chen, Y. Zhao, T. Chen, et al., "Correlation of Aspect Ratio of Montmorillonite Nanosheets with the Colloidal Properties in Aqueous Solutions," *Results in Physics* 15 (2019): 102526, https://doi.org/10.1016/j.rinp.2019.102526-/10.1016/j.rinp.2019.102526.

57. G. Laufer, C. Kirkland, A. A. Cain, and J. C. Grunlan, "Clay–Chitosan Nanobrick Walls: Completely Renewable Gas Barrier and Flame-Retardant Nanocoatings," *ACS Applied Materials & Interfaces* 4, no. 3 (2012): 1643–1649, https://doi.org/10.1021/am2017915.

58. K.Č. Barabaszová, G. S. Martynková, and K. Šulcová, "Mechanical Treated Vermiculite Particles: Surface and Size Characteristics," *Advanced Science Letters* 22, no. 3 (2016): 681–684, https://doi.org/10.1166/asl.2016.6903.

59. T. Dörres, M. Bartkiewicz, K. Herrmann, et al., "Nanoscale-Structured Hybrid Bragg Stacks with Orientation- and Composition-Dependent Mechanical and Thermal Transport Properties: Implications for Nacre Mimetics and Heat Management Applications," *ACS Applied Nano Materials* 5, no. 3 (2022): 4119–4129, https://doi.org/10.1021/acsanm.2c00061.

60. C. Prescher, C. McCammon, and L. Dubrovinsky, "MossA: A Program for Analyzing Energy-Domain Mossbauer Spectra from Conventional and Synchrotron Sources," *Journal of Applied Crystallography* 45, no. 2 (2012): 329–331, https://doi.org/10.1107/S0021889812004979-doi:10.1107/S0021889812004979.

61. S. Förster, S. Fischer, K. Zielske, et al., "Calculation of Scattering-Patterns of Ordered Nano- and Mesoscale Materials," *Advances in Colloid and Interface Science* 163, no. 1 (2011): 53–83, https://doi.org/10.1016/j.cis.2010.12.003.

Supporting Information

Additional supporting information can be found online in the supporting information section.